3-D Deformable Image Registration: A Topology Preservation Scheme Based on Hierarchical Deformation Models and Interval Analysis Optimization

Vincent Noblet, Christian Heinrich, Fabrice Heitz, and Jean-Paul Armspach

Abstract—This paper deals with topology preservation in three-dimensional (3-D) deformable image registration. This work is a nontrivial extension of [34], which addresses the case of two-dimensional (2-D) topology preserving mappings. In both cases, the deformation map is modeled as a hierarchical displacement field, decomposed on a multiresolution B-spline basis. Topology preservation is enforced by controlling the Jacobian of the transformation. Finding the optimal displacement parameters amounts to solving a constrained optimization problem: The residual energy between the target image and the deformed source image is minimized under constraints on the Jacobian. Unlike the 2-D case, in which simple linear constraints are derived, the 3-D B-spline-based deformable mapping yields a difficult (until now, unsolved) optimization problem. In this paper, we tackle the problem by resorting to interval analysis optimization techniques. Care is taken to keep the computational burden as low as possible. Results on multipatient 3-D MRI registration illustrate the ability of the method to preserve topology on the continuous image domain.

Index Terms—B-splines, deformable matching, global optimization, hierarchical parametric deformation models, interval analysis, three-dimensional (3-D) image registration, topology preservation, voxel–based registration.

I. INTRODUCTION

DEFORMABLE – intersubject – registration of three-dimensional (3-D) medical images has received considerable attention during the last decade [44], as a key step for the construction and use of individualized or probabilistic anatomical atlases [11], [17], [19], [42], [45]. Potential applications include atlas-based image segmentation and labeling [5], [17], [35], [36], [39], atlas-based image registration or fusion [36], motion analysis in 3-D image sequences [39], statistical analysis

of normal and pathological variations in anatomy [8], [30], [42], [43], follow-up of lesion evolution over time [6], [28], atlas-based volume estimation [1], [37], and the study of the growth and development of normal or abnormal anatomical structures [41], [43].

A desirable property of intersubject medical image warping is the preservation of the topology of anatomical structures since, in the continuous domain, anatomical structures have the same topology for any individual (at least for nonpathological cases) [4], [46]. Topology preservation ensures that connected structures remain connected and that the neighborhood relationship between structures is maintained. It also prevents the appearance or disappearance of existing or new structures. By enforcing this constraint, the space of possible solutions is restricted to physically acceptable deformations. Topology preservation is related to the continuity and invertibility of the transformation (which should be a homeomorphism or one-to-one mapping). This property is enforced by the positivity of the Jacobian of the transformation and the invariance of the boundary of the image [12], [34, Section 2 and Appendix C].

Thirion [39], [40] proposes a low-cost method for constraining the bijectivity property in a nonpreserving transformation. The method is based on the computation of the direct deformation T_{12} (from image 1 to image 2), the reverse deformation T_{21} (from image 2 to image 1) and the residual deformation $R = T_{21} \circ T_{12}$. To maintain bijectivity, the residual deformation is redistributed equally between T_{12} and T_{21} to obtain $R \simeq Id$. The method is fast and simple but does not mathematically ensure the preservation of the topology on the continuous image domain.

Topology preserving mappings have been considered by [10], [11], [13], [31], in the framework of viscous fluid models, corresponding to incompressible matter. The Navier–Stokes viscous-fluid partial derivative equations (PDEs) describing the physical medium are solved on a discrete spatial grid. This physical continuum model gives excellent results, allows both nonlinearities, large displacements and is topology preserving. Unfortunately, although topology preservation holds for the continuous transformation, it is no longer guaranteed when solving the PDE on the discrete image grid. It is, thus, necessary to check the Jacobian and to use a concatenation procedure consisting in propagating the floating image whenever the transformation becomes singular [13]. A similar tracking of the Jacobian is used in [42], [43], to control the volume transformation in a surface-based brain warping scheme. In [47], Trouvé restricts the

desired transformations to a subgroup of invertible mappings by exploiting Lie group theory. The problem is solved numerically using gradient descent and may be rewritten as a PDE, shown to be linked to the fluid model of Christensen [11]. Trouvé's model is more general and the associated numerical scheme is stable, so that no Jacobian tracking is needed. A related approach is used in [24] to match landmarks using large deformation diffeomorphisms.

Inspired by Grenander's General Pattern Theory [18], Miller and Younes [32] have recently devised a comprehensive framework for the representation of deformable templates. A deformable template (*e.g.,* an image to be warped) is an object on which a group of transformations acts, creating a whole family of new objects. The groups studied in [32] include finite dimensional matrix groups as well as infinite dimensional diffeomorphisms. The approach enables both variations in the geometry of the object (deformations) and in the images values themselves. It is also suited to both landmark and dense deformable matching.

A common framework for fast deformable matching of 3-D images is the linear decomposition of the transformation on hierarchical basis functions. The transformation is described by a limited number of parameters, yielding a significant reduction of the computational burden with respect to dense PDE-based approaches. For instance in [10], [16], [17], elastic matching is expressed as an expansion over a basis of Green's or sinusoidal functions, eigen-elements of the elastic operator. In [38], Szeliski introduces a hierarchical basis of spline interpolators for two-dimensional (2-D) nonrigid image registration. Chen *et al.* [8] extend this idea in 3-D for hierarchical matching of MR images. In [48] a Cai–Wang wavelet model is used to represent 2-D motion fields in image sequence analysis. A hierarchical spline representation, associated to a multiresolution representation of the deformation field over nested subspaces is considered in [33], [35]. A similar approach is described in [26], [27]. A robust estimation framework, associated to a hierarchical representation of the deformation field using piecewise affine models is proposed in [22].

Unfortunately, parametric deformation models relying on linear decompositions over basis functions do not by themselves enforce properties such as one-to-one mapping. Ashburner [2], [3] solves the issue for piecewise affine mappings, in a Bayesian framework, where the Gibbs potential associated to the prior distribution, is a function of the Jacobian. By penalizing noninvertible solutions through low probabilities, the mapping is ensured to preserve almost surely the topology. A similar approach is used in [9] with a 3-D Fourier representation, using a regularization framework to penalize small Jacobians.

A hard positivity constraint on the Jacobian has been implemented by the authors in 2-D, for a hierarchy of spline basis functions [34]. It is shown that the sign of the Jacobian on the *whole continuous* image domain may simply be controlled by linearly constraining the optimization on a finite number of points. In the present paper we extend this approach to the 3-D case. This extension is not trivial, due to the nonlinearity of the Jacobian in 3-D. Rather than simply constraining the positivity of the Jacobian, we devise a procedure allowing to enclose the Jacobian between two user-defined bounds. The resulting optimization problem is much more cumbersome than in 2-D and is tackled using interval analysis techniques. We employ a blockwise descent scheme. The main point is to determine the upper bound on the step in the line minimization procedure. The proposed approach guarantees the preservation of topology for the computed transformation on the whole continuous image domain (even though the image is only observed on a finite discrete spatial grid).

The paper is organized as follows. In Section II, the multiresolution deformation model and the underlying optimization problem are briefly presented (for details we refer to [34]). The interval analysis based procedure yielding the upper bound on the line minimization step for the optimization problem is detailed in the appendices. A number of examples on 3-D MR brain images are given in Section III to demonstrate how the method works. We also report on CPU times. Conclusions and perspectives are given in Section IV.

II. MULTIRESOLUTION DEFORMATION MODEL AND THE CORRESPONDING OPTIMIZATION PROBLEM

A. Multiresolution Deformation Model

Let $s \triangleq [x, y, z]^t \in \Omega$ and consider an image defined on $\Omega \subset \mathbb{R}^3$. The mapping $h \in \mathcal{H}$ between the source and the target image writes $h(s) = s + u(s)$, where u is the displacement vector field and $\mathcal{H}$ the Hilbert space of finite energy deformation fields.

We consider a decomposition of the displacement vector field u over a sequence of nested subspaces $V_0 \subset V_1 \subset \cdots \subset V_l \subset V_{l+1} \subset \cdots \subset \mathcal{H}$, defining a multiresolution approximation of u [29]. Space V_0 defines the coarsest scale representation. A basis of V_l may be generated from a scaling function Φ. To handle a 3-D deformation field, three multiresolution decompositions are considered, one for each component of the displacement. Every element of the basis of V_l writes

$$
\Phi_{i,j,k}^l(x,y,z) = \Phi_i^l(x) \, \Phi_j^l(y) \, \Phi_k^l(z)
$$
$$
= 2^{3l/2}\Phi(2^l x - i)\,\Phi(2^l y - j)\,\Phi(2^l z - k). \quad (1)
$$

At scale l, *i.e.,* in space V_l, the displacement field u^l will be parameterized by the vector $a^l \triangleq \left\{ a_{x;i,j,k}^l, a_{y;i,j,k}^l, a_{z;i,j,k}^l \right\}$ as

$$
u^l(x,y,z) = \begin{bmatrix} u_x^l(x,y,z) \\ u_y^l(x,y,z) \\ u_z^l(x,y,z) \end{bmatrix} = \begin{bmatrix} \sum\limits_{i,j,k} a_{x;i,j,k}^l \, \Phi_{i,j,k}^l(x,y,z) \\ \sum\limits_{i,j,k} a_{y;i,j,k}^l \, \Phi_{i,j,k}^l(x,y,z) \\ \sum\limits_{i,j,k} a_{z;i,j,k}^l \, \Phi_{i,j,k}^l(x,y,z) \end{bmatrix}.
$$
$$(2)$$

Only first-degree polynomial spline scaling functions Φ will be considered in this work (see Fig. 1), but the methods and algorithms used may be easily extended to higher degree B-spline functions (see Appendix I). Let $\Omega_{i,j,k}^l$ be the support of $\Phi_{i,j,k}^l$. We have

$$
\Omega_{i,j,k}^l = \left[\frac{i-1}{2^l}, \frac{i+1}{2^l} \right] \times \left[\frac{j-1}{2^l}, \frac{j+1}{2^l} \right] \times \left[\frac{k-1}{2^l}, \frac{k+1}{2^l} \right]
$$
$$
= \bigcup_{p,q,r} S_{p,q,r}^l
$$

where

$$
S_{p,q,r}^l = \left[\frac{p}{2^l}, \frac{p+1}{2^l} \right] \times \left[\frac{q}{2^l}, \frac{q+1}{2^l} \right] \times \left[\frac{r}{2^l}, \frac{r+1}{2^l} \right]
$$

and $p \in \{i-1; i\}; q \in \{j-1; j\}; r \in \{k-1; k\}$ (see Fig. 2). The displacement fields are nested: Any deformation field at

$$\Phi_i^l(x) = 2^{l/2} \, \phi(2^l \, x - i)$$

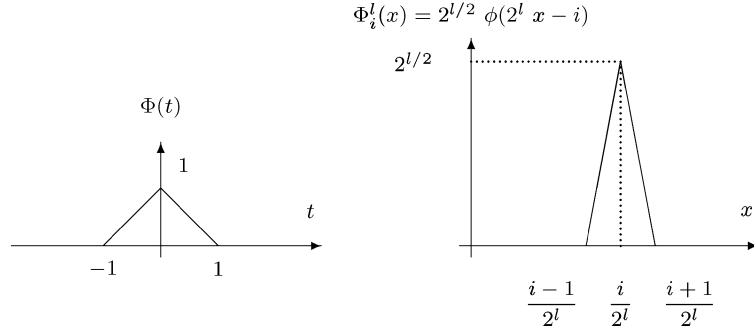Fig. 1.   Polynomial spline scaling function $\Phi(t)$ of degree 1 and a corresponding basis vector $\Phi_i^l(x)$.
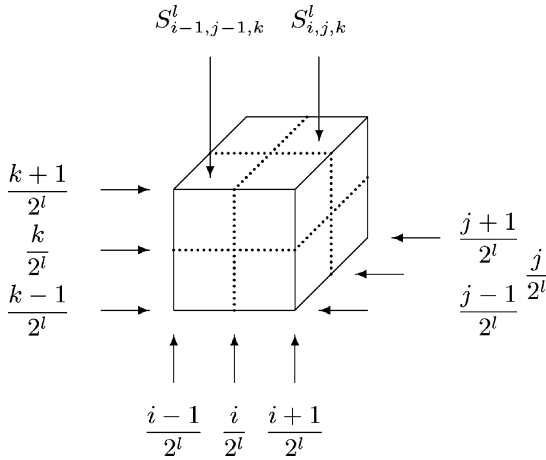

Fig. 2.   Box $\Omega_{i,j,k}^l$ and related $S_{p,q,r}^l$s subboxes.

scale l may also be expressed as a deformation field at a finer scale $l+1$ [29], [34].

B. Underlying Optimization Problem

The cost function E related to the displacement field $\boldsymbol{u}$ is defined as $E(\boldsymbol{u}) \triangleq \int_\Omega |I_1(\boldsymbol{s}) - I_2(\boldsymbol{h}(\boldsymbol{s}))|^2 \, d\boldsymbol{s}$, where I_1 is the target image and I_2 the source image. For a given scale l, the optimization problem writes: $\widehat{\boldsymbol{a}}^l = \arg \min_{\boldsymbol{a}^l \in \mathcal{A}^l} E(\boldsymbol{u})$, where $\mathcal{A}^l$ stands for the admissible parameter set. The energy landscape E is highly multimodal. Iterating on the scale l in a coarse to fine sequence of displacements (see Section II-D) is the means of (hopefully) escaping local minima at an acceptable computational cost (as opposed to using stochastic algorithms leading to an unacceptably high-computational cost for the problem at hand). At scale $l+1$, the optimization procedure is initialized with the solution of the optimization problem at scale l (see Fig. 3).

We apply a blockwise descent algorithm, the mth block being $\left[a_{x;i,j,k}^l, a_{y;i,j,k}^l, a_{z;i,j,k}^l \right]$, for given values of i, j, k. Inside the block, the direction of descent $\boldsymbol{d} \in \mathbb{R}^3$ is computed as the opposite of the gradient $\partial E / \partial \boldsymbol{a}^l$ of the cost function E where

$$\frac{\partial E}{\partial \boldsymbol{a}^l} = \int_\Omega \left(\frac{\partial \boldsymbol{h}}{\partial (\boldsymbol{a}^l)^t} \right)^t \frac{\partial I_2}{\partial \boldsymbol{s}} \bigg|_{\boldsymbol{s} = \boldsymbol{h}(\boldsymbol{s})} 2 \left(I_2(\boldsymbol{h}(\boldsymbol{s})) - I_1(\boldsymbol{s}) \right) \, d\boldsymbol{s}.$$

During the line minimization, the cost function only needs to be evaluated on $\Omega_{i,j,k}^l$ since this function is not modified outside $\Omega_{i,j,k}^l$. Moreover, there exists an upper bound on the step size, above which the bounding conditions on the Jacobian are not verified (see Section II-C). The complete optimization algorithm is given below in Section II-D.

C. Admissible Parameter Set

The admissible parameter set $\mathcal{A}^l$ is the set of all coordinate vectors $\boldsymbol{a}^l$ yielding admissible values of the Jacobian J over Ω, i.e.

$$\forall [x, y, z]^t \in \Omega \quad J\left(x, y, z, \boldsymbol{a}^l\right) \in [J_m, J_M] \tag{3}$$

where

$$J\left(x, y, z, \boldsymbol{a}^l\right) = \det \begin{bmatrix} \frac{\partial h_x^l}{\partial x} & \frac{\partial h_x^l}{\partial y} & \frac{\partial h_x^l}{\partial z} \\ \frac{\partial h_y^l}{\partial x} & \frac{\partial h_y^l}{\partial y} & \frac{\partial h_y^l}{\partial z} \\ \frac{\partial h_z^l}{\partial x} & \frac{\partial h_z^l}{\partial y} & \frac{\partial h_z^l}{\partial z} \end{bmatrix}$$

$$\boldsymbol{h}^l(x, y, z) = \begin{bmatrix} h_x^l(x, y, z) \\ h_y^l(x, y, z) \\ h_z^l(x, y, z) \end{bmatrix} = \begin{bmatrix} x + u_x^l(x, y, z) \\ y + u_y^l(x, y, z) \\ z + u_z^l(x, y, z) \end{bmatrix}$$

and J_m and J_M are user-defined bounds (for topology preservation, J_m must be set to positive values).

In the case of a blockwise descent, condition 3 needs only to be checked on the box $\Omega_{i,j,k}^l$ since the parameters to be modified do not affect $\Omega \setminus \Omega_{i,j,k}^l$. The box $\Omega_{i,j,k}^l$ will be partitioned in $S_{p,q,r}^l$–type subboxes, and condition 3 will be checked on those subboxes. Attention will now be focused on $S_{p,q,r}^l$, leading eventually to the expression of the Jacobian on $S_{p,q,r}^l$.

The basis functions $\Phi_{p,q,r}^l, \Phi_{p,q,r+1}^l, \ldots, \Phi_{p+1,q+1,r+1}^l$ are impinging on box $S_{p,q,r}^l$ and, to compute the Jacobian on $S_{p,q,r}^l$, the indexes spanning the sums in (2) may be restricted to the sets: $i = p, p+1; j = q, q+1; k = r, r+1$.

Let us define (see Fig. 4)

$$\begin{cases} p^+(t, n, l) & \triangleq & 2^{l/2} \left(2^l \, t - n \right), \\ p^-(t, n, l) & \triangleq & -2^{l/2} \left(2^l \, t - (n+1) \right). \end{cases}$$
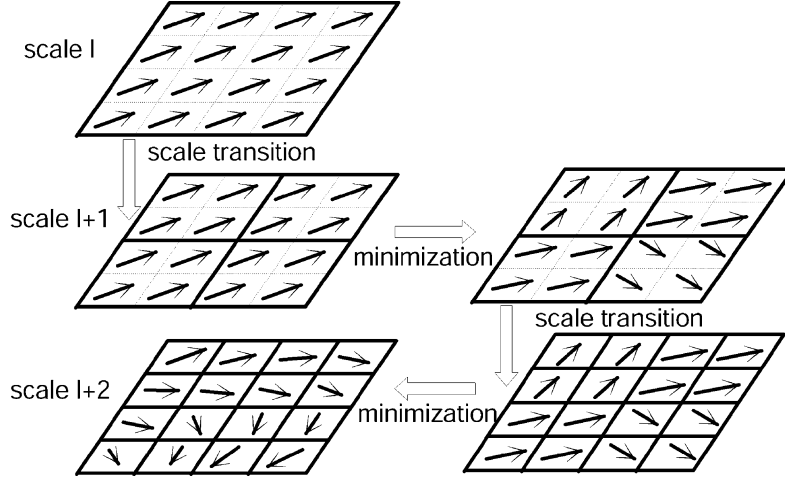
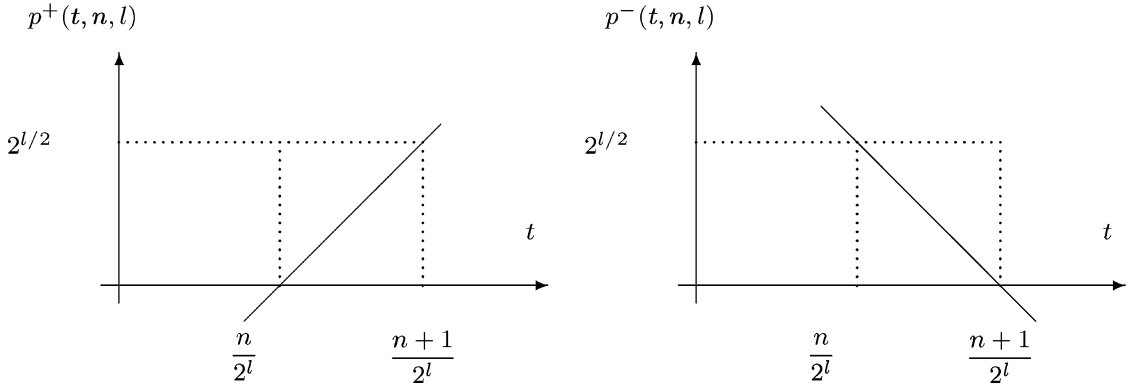Fig. 3.   Hierarchical optimization procedure in the 2-D case for the spline of degree 0 (Haar basis).

Fig. 4.   Linear functions p^- and p^+ as elementary components yielding $\boldsymbol{u}^l$.

It is straightforward [see (1) and (2)] that on $S_{p,q,r}^l$, we have

$$
\begin{aligned}
u_x^l\,(x,y,z) = \\
a_{x;p,q,r}^l \quad & p^-\,(x,p,l) \quad p^-\,(y,q,l) \quad p^-\,(z,r,l) \\
+\quad a_{x;p,q,r+1}^l \quad & p^-\,(x,p,l) \quad p^-\,(y,q,l) \quad p^+\,(z,r,l) \\
\vdots \\
+\quad a_{x;p+1,q+1,r+1}^l \quad & p^+(x,p,l) \quad p^+(y,q,l) \quad p^+(z,r,l).
\end{aligned}
$$

The same kind of expressions hold for u_y^l and u_z^l. With the help of a symbolic computation software, we get

$$
\begin{aligned}
J\,(x,y,z,\boldsymbol{\alpha}) = {} & \alpha_1 + \alpha_2\,x + \alpha_3\,y + \alpha_4\,z + \alpha_5\,x^2 + \alpha_6\,x\,y \\
& + \alpha_7\,x\,z + \alpha_8\,y^2 + \alpha_9\,y\,z + \alpha_{10}\,z^2 \\
& + \alpha_{11}\,x^2\,y + \alpha_{12}\,x^2\,z + \alpha_{13}\,x\,y^2 \\
& + \alpha_{14}\,x\,y\,z + \alpha_{15}\,x\,z^2 + \alpha_{16}\,y^2\,z + \alpha_{17}\,y\,z^2 \\
& + \alpha_{18}\,x^2\,y\,z + \alpha_{19}\,x\,y^2\,z + \alpha_{20}\,x\,y\,z^2
\end{aligned}
$$

where the α_is are polynomial expressions of the components of $\boldsymbol{a}^l$ involved in $S_{p,q,r}^l$. Moreover, it may be easily shown that any α_i is an affine function of any set $[a_{x;n_1,n_2,n_3}^l,\ a_{y;n_1,n_2,n_3}^l,\ a_{z;n_1,n_2,n_3}^l]$ (see Appendix I). Considering that the blockwise descent takes place along

direction $\boldsymbol{d}$ ($\boldsymbol{d}$ is a coordinate vector defined on the space $[a_{x;n_1,n_2,n_3}^l\ a_{y;n_1,n_2,n_3}^l\ a_{z;n_1,n_2,n_3}^l]$) with a step δ, we may express the Jacobian as

$$
\begin{aligned}
J(x,&y,z,\delta) \\
= {} & \left(\beta_1^a + \delta\beta_1^b\right) + \left(\beta_2^a + \delta\beta_2^b\right) x + \left(\beta_3^a + \delta\beta_3^b\right) y \\
& + \left(\beta_4^a + \delta\beta_4^b\right) z + \left(\beta_5^a + \delta\beta_5^b\right) x^2 + \left(\beta_6^a + \delta\beta_6^b\right) xy \\
& + \left(\beta_7^a + \delta\beta_7^b\right) xz + \left(\beta_8^a + \delta\beta_8^b\right) y^2 + \left(\beta_9^a + \delta\beta_9^b\right) yz \\
& + \left(\beta_{10}^a + \delta\beta_{10}^b\right) z^2 + \left(\beta_{11}^a + \delta\beta_{11}^b\right) x^2 y + \left(\beta_{12}^a + \delta\beta_{12}^b\right) x^2 z \\
& + \left(\beta_{13}^a + \delta\beta_{13}^b\right) xy^2 + \left(\beta_{14}^a + \delta\beta_{14}^b\right) xyz + \left(\beta_{15}^a + \delta\beta_{15}^b\right) xz^2 \\
& + \left(\beta_{16}^a + \delta\beta_{16}^b\right) y^2 z + \left(\beta_{17}^a + \delta\beta_{17}^b\right) yz^2 + \left(\beta_{18}^a + \delta\beta_{18}^b\right) x^2 yz \\
& + \left(\beta_{19}^a + \delta\beta_{19}^b\right) xy^2 z + \left(\beta_{20}^a + \delta\beta_{20}^b\right) xyz^2.
\end{aligned}
$$

For higher order splines, J remains an affine function of δ when x, y, z are fixed (see Appendix I), and, thus, the following method may be adapted.

Let us define

$$
\begin{cases}
J_m\,(\delta) \triangleq \displaystyle\inf_{[x,y,z]^t \in S_{p,q,r}^l} J\,(x,y,z,\delta) \\[2mm]
J_M\,(\delta) \triangleq \displaystyle\sup_{[x,y,z]^t \in S_{p,q,r}^l} J\,(x,y,z,\delta).
\end{cases}
$$
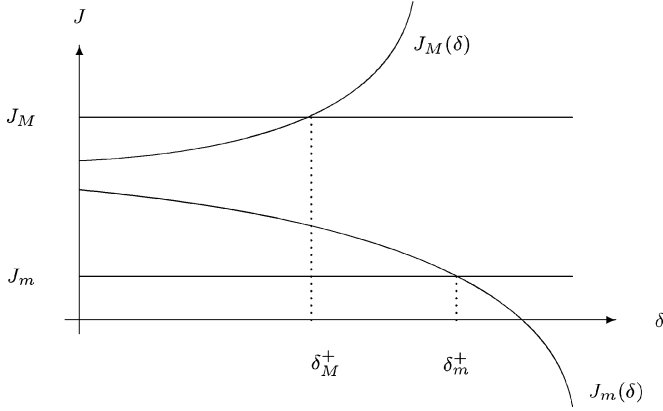
Fig. 5. Bound δ^+ is computed as a lower bound of $\inf\{\delta_M^+, \delta_m^+\}$.
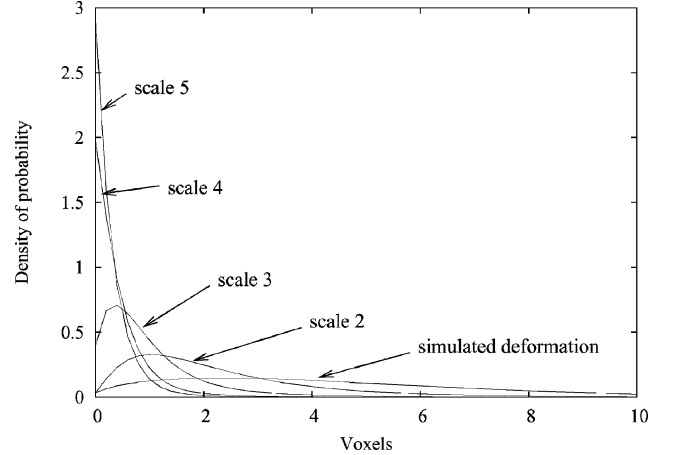

Fig. 6. Density of probability of the $\mathcal{L}_2$ norm of the displacement error at different scales. As expected, the displacement error concentrates toward the origin as the scale increases. At scale 5, more than 96% of the voxels are affected by an error lower than 1 voxel.

Admissible steps δ are such that

$$J_m \le J_m\left(\delta\right) \le J_M\left(\delta\right) \le J_M. \tag{4}$$

The Jacobian values $J_m\left(0\right)$ and $J_M\left(0\right)$ also match condition 4, since they are the result of a previous optimization step enforcing this very condition. Moreover, it is straightforward that $J_m\left(\delta\right)$ is concave and $J_M\left(\delta\right)$ is convex (as the infimum and supremum of a set of affine functions). Hence, the set of admissible values of δ is convex and determining the admissible steps amounts to determining the upper bound δ^+ of this set (see Fig. 5).

Since δ^+ is defined considering $S_{p,q,r}^l$, we get a set of eight δ^+s ($\Omega_{i,j,k}^l$ encloses eight subboxes, see the beginning of this section). The effective bound is derived as the infimum of this set.

D. Summing Things Up

The optimization algorithm eventually writes:

Optimization algorithm yielding $\widehat{a}$
```
Loop on scale l
 compute a^l from â^{l-1}
 do
  loop on i,j,k
// update of {a^l_{x;i,j,k}, a^l_{y;i,j,k}, a^l_{z;i,j,k}}
   compute direction of descent d
   compute δ^+
   update a^l by minimization of E along d
with a step δ̂ ∈ [0,δ^+]
  end loop on i,j,k
 until convergence of a^l
end loop on scale l.
```

The most cumbersome problem at this point is the computation of δ^+ to devise an algorithm yielding the maximal admissible step

$$\delta^+ = \sup\left\{\delta \,\middle|\, \forall\,[x,y,z]^t \in \Omega_{i,j,k}^l \;\; J_m \le J\left(x,y,z,\delta\right) \le J_M\right\}$$

along the direction of descent while keeping the computational burden as low as possible.

The Jacobian J as a function of x, y, z on a given $S_{p,q,r}^l$ box has no nice property such as convexity and may have local minima and maxima. Hence, we have to resort to a global optimization algorithm. Interval analysis techniques are well suited to the case at hand. A general flavor of such techniques is given in Appendix III. We refer the reader to [23] for more details.

The main objective is to bracket δ^+, *i.e.*, to determine δ_i^+ and δ_s^+ reasonably close enough such that $\delta^+ \in \left[\delta_i^+; \delta_s^+\right]$. This is achieved in two steps (initialization and refinement) in the interval analysis framework. The details of this quite technical procedure are developed in Appendix II to which the interested reader is referred.

III. ILLUSTRATION ON 3-D BRAIN IMAGE REGISTRATION

The contribution of topology preservation is illustrated here on 3-D MR brain image registration. The assessment of inter-subject (deformable) image warping is a delicate problem, due to the general lack of ground truth. The general behavior of the method is first assessed using a simulated deformation field playing the role of a ground truth. The method is then applied to real registration problems where no ground truth is available.

A. Method Performance Assessment Using a Simulated Ground Truth

The general behavior of the method is assessed using simulated deformation fields. A topology preserving blockwise sinusoidal transformation is applied to a 3-D image, hence creating a ground truth. The transformation is chosen to be blockwise sinusoidal so that it cannot be perfectly matched with a B-spline based transformation at the scales envisaged.

The estimated transformation field at a given scale may be compared to the sought transformation using an error vector

TABLE I
CPU TIME AND DISPLACEMENT ERROR AT SUCCESSIVE SCALES. IT MUST BE NOTICED THAT THE VALUE OF THE COST FUNCTION
HAS NO PARTICULAR MEANING, SINCE IT DEPENDS ON THE SIZE OF THE IMAGE AND ON THE RANGE OF THE GRAY VALUES

Scale l	Number of block updates	Total CPU time (seconds)	Cost function	Mean displacement error (voxels)	Median displacement error (voxels)
Initial state			$21.2\ 10^5$	4.30	3.62
1	1	11	$19.7\ 10^5$	4.13	2.75
2	40	54	$14.8\ 10^5$	2.18	1.54
3	465	115	$9.19\ 10^5$	0.90	0.45
4	2506	169	$6.35\ 10^5$	0.33	0.25
5	14034	313	$5.54\ 10^5$	0.19	0.17

TABLE II
INFLUENCE OF THE BOUNDS J_m, J_M ON THE DISPLACEMENT OF THE ESTIMATED FIELD

J_m	J_M	Cost function	Mean displacement (voxels)	Median displacement (voxels)
0	100000	$5.43\ 10^5$	8.9	7.2
0.5	2	$7.64\ 10^5$	8.5	7.1
0.8	1.2	$18.0\ 10^5$	3.1	2.6
0.9	1.1	$20.0\ 10^5$	1.3	1.0

field (the error vector field is the difference between the estimated and the sought fields). The mean distributions[1] of the $\mathcal{L}_2$ norm of the displacement error at each foreground voxel for different scales ($l = 2, \ldots 5$) are depicted Fig. 6. The CPU time and displacement errors at successive scales related to those simulations are reported Table I. As expected, the registration gets more precise as the scale increases, since the set of authorized transformations enlarges.

It may be noticed that about 85% of the total CPU time of a registration up to scale 5 is dedicated to computation of the bounds δ^+. At scale 6 (CPU time: 30 min), the cost function still decreases but the displacement error gets worse since interpolation artifacts become nonnegligible in the registration process (they are no longer averaged out).

The effect of the bounds J_m, J_M may be illustrated considering the mean displacement of the estimated field (see Table II, see also Fig. 8). As expected, moving the bounds J_m and J_M toward 1 increases the registration error and decreases the mean displacement: The set of authorized transformations is reduced since the constraints are more severe and large displacements expected for a precise registration are no longer tolerated because they are no longer compatible with the condition on the Jacobian bounds.

B. Real Case Brain Image Registration

No ground truth is available in this case to evaluate the quality of registration. Mere visual inspection of gray levels is mis-

leading for such an evaluation. Gray levels tend to be similar, since the residual energy is minimized during the optimization procedure. As a consequence, a perfect matching of gray levels does not necessarily mean that the registration is relevant, since the deformation field may have no physical meaning, *i.e.,* the topology of brain structures may not be preserved. The deformation field has to be examined, in conjuction with gray levels. This may be achieved for example by warping a synthetic grid using the estimated transformation. To highlight the contribution of topology preservation, we also consider the warping of anatomical atlases, which is a standard procedure to produce automatic segmentations in medical images.

Fig. 7 displays the results of a 3-D interindividual deformable registration: Fig. 7(a) is registered on Fig. 7(d) without any constraint [Fig. 7(b)] and with the positivity constraint on the Jacobian [Fig. 7(c)]. To enlighten the effect of topology preservation, both resulting deformation fields are applied to a regular grid located in the interhemispheric plan (Fig. 8). The deformation field obtained from a registration with no constraint leads to a tearing of the mesh[2] [Fig. 8(b)], which proves topology violation. Violations of topology mainly concern regions:

- around the mouth because of the movement caused by breathing;
- around the neck because of the lack of information in this region in one of the images.

---

[1]Nine different registrations have been achieved and their distributions averaged.

[2]In fact, no tearing may happen with the transformation at hand since this transformation is necessarily continuous. Only folding is involved when topology is violated. Folding has the same visual effect as tearing. In the sequel, we will only speak about tearing for the sake of simplicity.
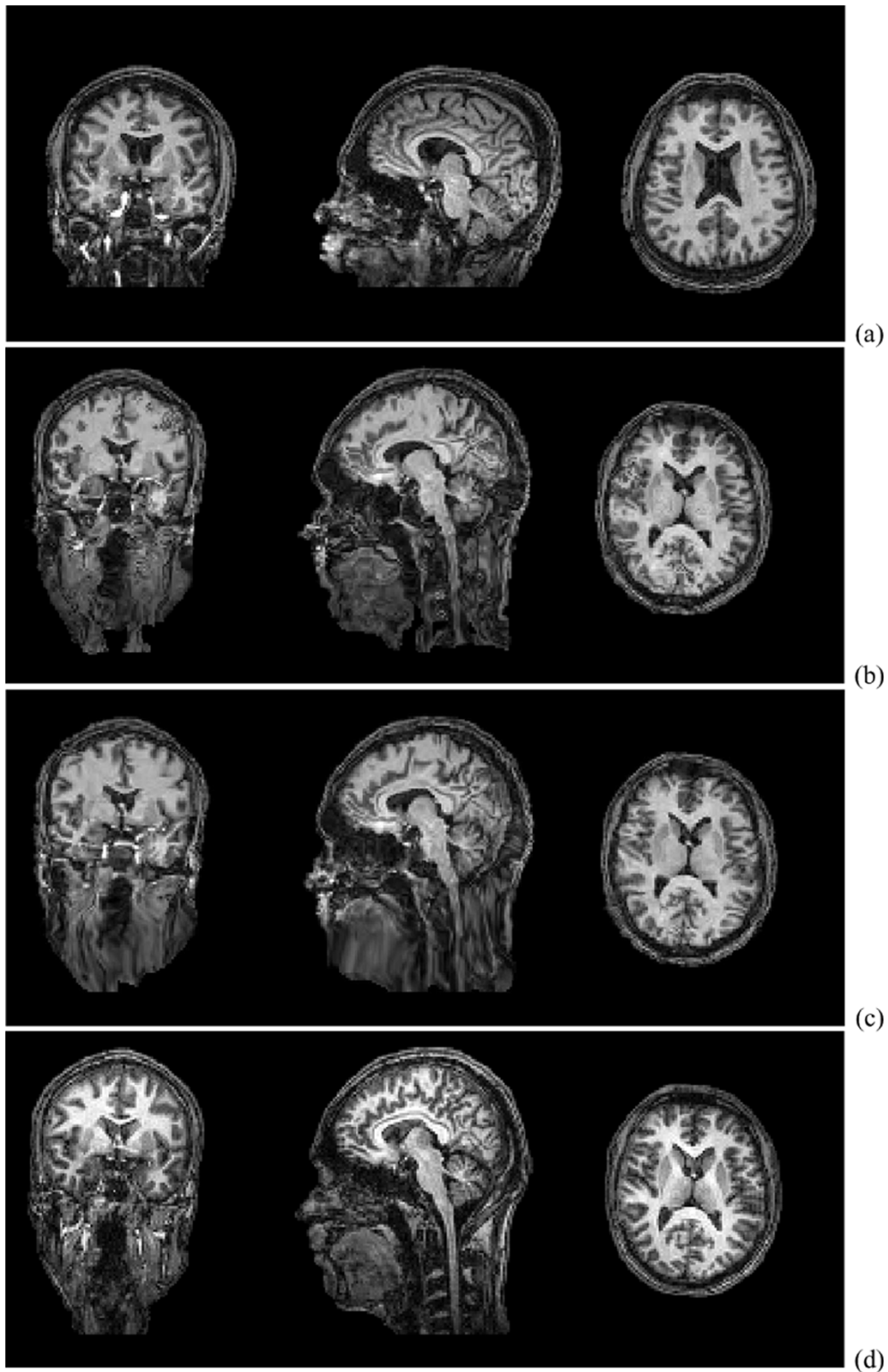
Fig. 7.   Nonrigid matching of MR images from two different individuals. (a) Source image. (b) Result of the deformable matching without any constraint. (c) Result of the deformable matching with the positivity contraint $J > 0$. (d) Target image.

Imposing a positivity constraint on the Jacobian regularizes the deformation field [Fig. 8(c)] and avoids tearing of the mesh.

Another good illustration of the contribution of topology preservation is observed on atlas-based MRI segmentation (Fig. 9). Atlas-based segmentation consists in registering a patient MRI on a reference MRI, associated to a 3-D reference segmentation map (the atlas). The atlas is then warped on the patient data, using the estimated deformable mapping [5], [17], [35], [36]. Atlas warping is one of the most robust method for performing automatic segmentation of anatomical structures but it is sensitive to the quality of the reference segmentation as well as to registration errors or to violations of the topology
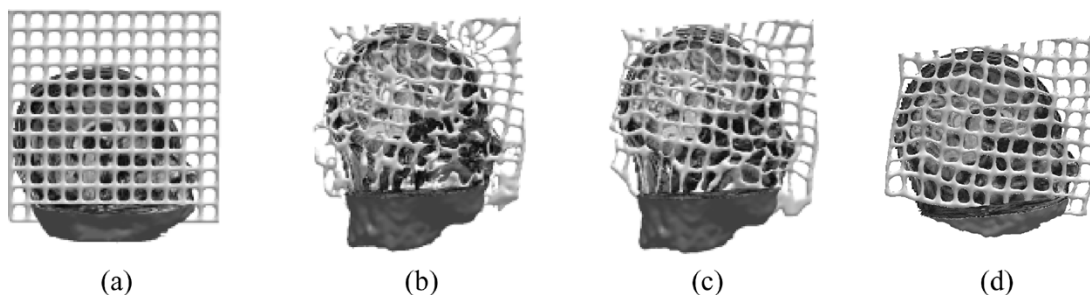
Fig. 8.   Visualization of the deformation field on a regular grid placed in the interhemispheric plan. (a) Source image. (b) Grid warped without any constraint. (c) Grid warped with the positivity constraint $J > 0$. (d) Grid warped with the constraint $0.5 < J < 2$. As expected, the deformation field is much smoother in (d) than (c).
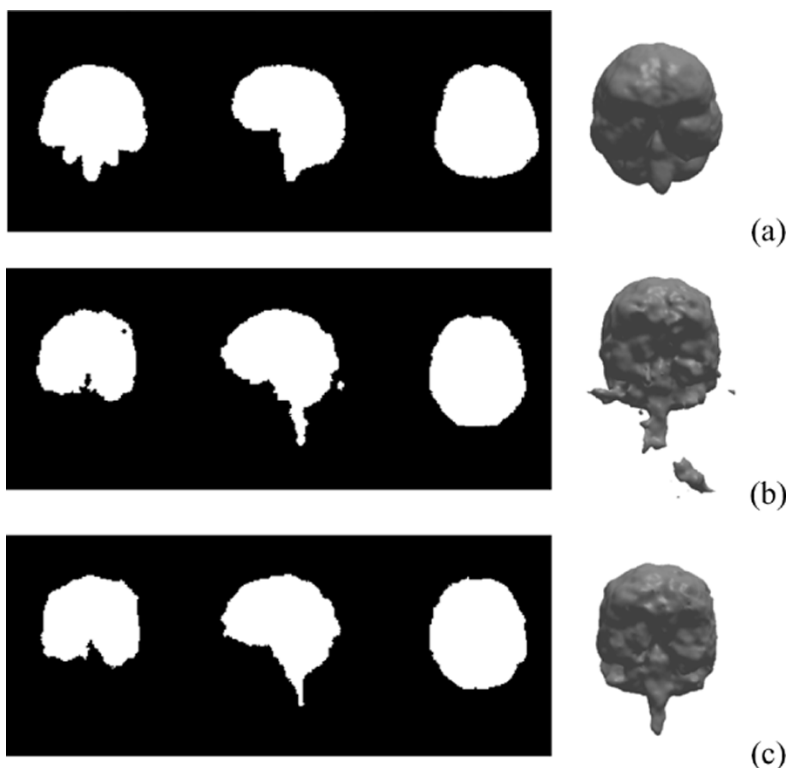

Fig. 9.   Application to atlas-based automatic brain segmentation. (a) Reference brain mask (atlas). (b) Brain mask warped without any constraint. (c) Brain mask warped with the positivity constraint $J > 0$.

of the underlying anatomical structures. Holes and tearing are present in the warped segmentation brain mask when no constraint is imposed as may be seen on Fig. 9(b). Fig. 10 shows another example of topology violation during registration in an atlas-based segmentation attempt. The violation is illustrated by a tearing of ventricles.

We also registered both images using a cost function including a term penalizing the Jacobian as

$$\begin{cases} E_J(J) = \infty, & \text{if } J \leq 0 \\ E_J(J) = 0, & \text{if } J > 0. \end{cases}$$

The registration result was visually very close to the registration obtained when enforcing positivity of the Jacobian on the underlying continuous space. The CPU time was five times lower. Nevertheless, the positivity of the Jacobian was no longer verified between voxel sites, which may cause a problem especially when registering low-resolution images and applying the resulting transformation to higher resolution images.

All the registrations were performed on 3-D 128^3 MR brain images up to scale $l = 5$ (which corresponds to $90\,000$ parameters) with a computational burden lower than 15 min for real clinical cases on a 2.4-GHz PC workstation (a Levenberg-Marquardt descent algorithm was used). Let us notice that the computation time is larger for real registrations than for registrations using simulated deformation fields (see Table I). Trilinear interpolation was used in all cases.

IV. CONCLUSION AND PERSPECTIVES

In this article, we have devised a procedure allowing topology preservation for the registration of 3-D images. We considered a hierarchical B-spline deformation field model. Topology preservation on the whole continuous domain is enforced by a positivity constraint on the Jacobian of the transformation. More
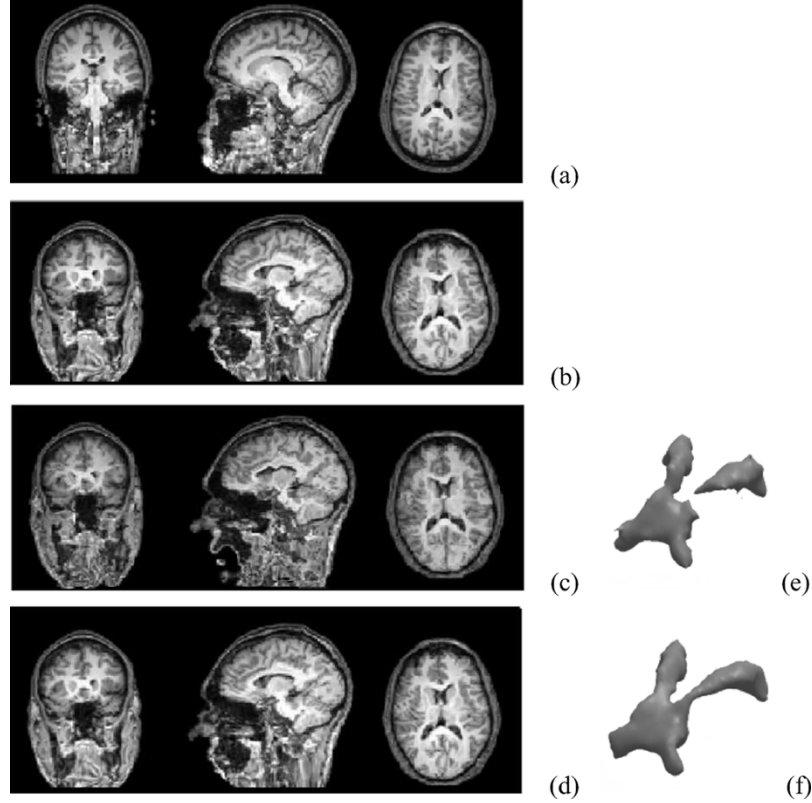
Fig. 10. Nonrigid matching between two different patients and application to atlas-based ventricle segmentation. (a) Source image. (b) Target image. (c) Result of matching without any constraint. (d) Result of matching with the positivity constraint $J > 0$. (e) Segmented registered ventricle without any constraint. (f) Segmented registered ventricle with the positivity constraint.

generally, we sought to enclose the Jacobian between two user-defined bounds.

The optimal registration map is found by minimizing the residual energy between the warped source image and the target image. Taking into account the bounding conditions on the Jacobian amounts to considering constraints in the optimization problem: We apply a blockwise descent scheme where an upper bound on the displacement step has to be determined. Determining this bound involves a cumbersome optimization problem in the 3-D image case which is solved using interval analysis techniques. Registration results are given, which were obtained at an acceptable computational cost.

Three perspectives to this work may be given. First, the cost function should be modified from

$$E\left(\boldsymbol{u}\right) = \int_{\Omega} \left|I_1\left(\boldsymbol{s}\right) - I_2\left(\boldsymbol{h}\left(\boldsymbol{s}\right)\right)\right|^2 \, d\boldsymbol{s}$$

to

$$\begin{aligned} E\left(\boldsymbol{u}\right) &= \int_{\Omega} \left|I_1\left(\boldsymbol{s}\right) - I_2\left(\boldsymbol{h}\left(\boldsymbol{s}\right)\right)\right|^2 \, \frac{1}{2} \, \left(d\boldsymbol{s} + d\boldsymbol{h}\right) \\ &= \int_{\Omega} \left|I_1\left(\boldsymbol{s}\right) - I_2\left(\boldsymbol{h}\left(\boldsymbol{s}\right)\right)\right|^2 \, \frac{1}{2} \, \left(1 + |J|\right) \, d\boldsymbol{s}. \end{aligned}$$

This stems from the fact that both images do not play a symmetrical role when considering the current version of the energy: The energy is computed with respect to a uniform inte-

gration measure $d\boldsymbol{s}$ with respect to the target image I_1 and considering one image or the other one as the target image will not give registration maps which are inverse of each other, which is unsatisfactory. The integration measure should be modified so as to be symmetrical with respect to both images, which is achieved by the measure $(1/2) \, (d\boldsymbol{s} + d\boldsymbol{h})$ (see also [7]). This modification of the cost function has no influence on the determination of the bound of the displacement step and, hence, may be straightforwardly incorporated in the proposed topology preserving procedure.

A second and more demanding perspective is topology-preserving registration of multimodal images, where corresponding voxels are linked by intensities which are not necessarily similar. This will lead to questioning the choice of the function to be optimized.

Finally, comparisons with other nonrigid registration techniques should be achieved in the spirit of [21]. Quantitative techniques [wavelet analysis of image registration (WAIR) [14], [15] and canonical variate analysis (CVA) [25]] for comparing registration methods have recently been proposed.

APPENDIX I
JACOBIAN IS AN AFFINE FUNCTION OF THE DISPLACEMENT STEP

In this Appendix, we show that the Jacobian $J\left(x, y, z, \delta\right)$ is an affine function of the displacement step δ when x, y, z are fixed. This property holds whatever the spline Φ considered.
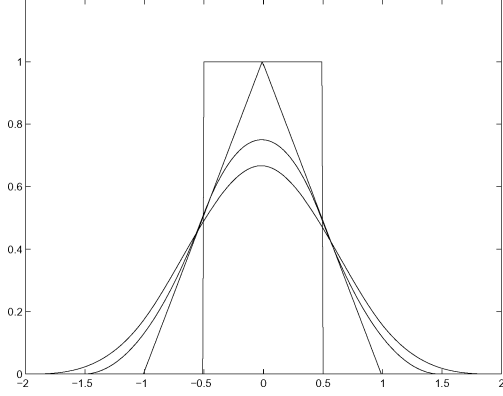
Fig. 11. Polynomial spline scaling functions of degree 0, 1, 2, 3.

Considering (2) and the blockwise descent scheme (descent takes place on the block $\left[a^l_{x;i,j,k}\ a^l_{y;i,j,k}\ a^l_{z;i,j,k}\right]$), the coordinates of the displacement field write

$$
\begin{cases}
u^l_x(x,y,z) &= a^l_{x;i,j,k}\ \Phi^l_{i,j,k}(x,y,z) + P_x(x,y,z) \\
u^l_y(x,y,z) &= a^l_{y;i,j,k}\ \Phi^l_{i,j,k}(x,y,z) + P_y(x,y,z) \\
u^l_z(x,y,z) &= a^l_{z;i,j,k}\ \Phi^l_{i,j,k}(x,y,z) + P_z(x,y,z)
\end{cases}
$$

where P_x, P_y, P_z are functions which may be computed straightforwardly from (2). The Jacobian may be expressed as shown in the equation at the bottom of the page.

It may be shown that J is a first-order polynomial in the block-variables $\left[a^l_{x;i,j,k}\ a^l_{y;i,j,k}\ a^l_{z;i,j,k}\right]$ (all higher order terms cancel out) which may be written $J = \mu_0 + \mu_x\ a^l_{x;i,j,k} + \mu_y\ a^l_{y;i,j,k} + \mu_z\ a^l_{z;i,j,k}$. Besides, block $\left[a^l_{x;i,j,k}\ a^l_{y;i,j,k}\ a^l_{z;i,j,k}\right]$ is updated along direction $\boldsymbol{d} \triangleq [d_x\ d_y\ d_z]^t$ as $\left[a^l_{x;i,j,k}\ a^l_{y;i,j,k}\ a^l_{z;i,j,k}\right] \longleftarrow \left[a^l_{x;i,j,k}\ a^l_{y;i,j,k}\ a^l_{z;i,j,k}\right] + \delta\ \boldsymbol{d}^t$. The Jacobian J then reads

$$
J = \mu_0 + \mu_x\left(a^l_{x;i,j,k} + \delta d_x\right) + \mu_y\left(a^l_{y;i,j,k} + \delta d_y\right) \\
+ \mu_z\left(a^l_{z;i,j,k} + \delta d_z\right)
$$

which proves that J is an affine function of the displacement step δ.

We may also give some hints on how to extend the algorithm to higher degree B-splines. We will consider the case of a second-order degree spline Φ_2 (see Fig. 11) for the sake of simplicity, but the extension to higher degree splines is straightforward.

Let $\Phi_2 = \Phi_0 \star \Phi_0 \star \Phi_0$ where Φ_0 is the rectangle function (the box spline). The spline Φ_2 is a piecewise second-degree poly-

nomial, where p^{-1}, p^0, p^{+1} are the second-degree polynomials playing the role of p^-, p^+ is the first-degree case. The support $\Omega^l_{i,j,k}$ of $\Phi^l_{i,j,k}$ is split into $3 \times 3 \times 3 = 27\ S^l$–type subboxes. Hence, the proposed algorithm still holds, the main modification being in the number of subboxes to be considered when updating a block of variables.

APPENDIX II
DETERMINATION OF THE MAXIMAL ADMISSIBLE STEP ALONG THE DIRECTION OF DESCENT

The goal of this Appendix is to propose an algorithm yielding the maximal admissible step

$$
\delta^+ = \sup\left\{\delta \left| \forall [x,y,z]^t \in \Omega^l_{i,j,k}\ \ J_m \le J(x,y,z,\delta) \le J_M \right.\right\}
$$

along the direction of descent while keeping the computational burden as low as possible.

The main objective is to bracket δ^+, $i.e.$, to determine δ_i^+ and δ_s^+ reasonably close enough such that $\delta^+ \in \left[\delta_i^+; \delta_s^+\right]$. This is achieved in two steps (initialization and refinement) which are detailed in the sequel.

A. Preliminaries

As usual in the interval analysis framework, $J_m(\delta)$ and $J_M(\delta)$ will not be computed but bracketed. We, thus, consider functions $J_M^+(\delta), J_M^-(\delta), J_m^+(\delta)$ and $J_m^-(\delta)$ such that

$$
\begin{cases}
J_M(\delta) &\in \left[J_M^-(\delta), J_M^+(\delta)\right] \\
J_m(\delta) &\in \left[J_m^-(\delta), J_m^+(\delta)\right].
\end{cases}
$$

Processing of $J_m(\delta)$ and $J_M(\delta)$ are akin. Hence, we will only deal with the former one in the sequel when both are to be addressed.

The interval analysis based global optimization algorithm yields $J_m^-(\delta), J_m^+(\delta)$ and a point N such that

$$
\begin{cases}
J_m^-(\delta) \le J_m(\delta) \le J_m^+(\delta), \\
J(N_x, N_y, N_z, \delta) = J_m^+(\delta).
\end{cases}
$$

The overall precision of the procedure ($i.e.$, $J_m^+(\delta) - J_m^-(\delta)$ and, as a consequence, $\delta_s^+ - \delta_i^+$) is user-controlled.

B. Initialization Step

The goal of the initialization step is to give quickly a relevant upper bound δ_s^+ of δ^+, so that the refinement step may proceed. Particular points in $\Omega^l_{i,j,k}$ will be picked and the corresponding Jacobians considered, possibly giving upper bounds on δ^+.

$$
J = \det\begin{bmatrix}
1 + a^l_{x;i,j,k}\frac{\partial\Phi^l_{i,j,k}}{\partial x} + \frac{\partial P_x}{\partial x} & a^l_{x;i,j,k}\frac{\partial\Phi^l_{i,j,k}}{\partial y} + \frac{\partial P_x}{\partial y} & a^l_{x;i,j,k}\frac{\partial\Phi^l_{i,j,k}}{\partial z} + \frac{\partial P_x}{\partial z} \\
a^l_{y;i,j,k}\frac{\partial\Phi^l_{i,j,k}}{\partial x} + \frac{\partial P_y}{\partial x} & 1 + a^l_{y;i,j,k}\frac{\partial\Phi^l_{i,j,k}}{\partial y} + \frac{\partial P_y}{\partial y} & a^l_{y;i,j,k}\frac{\partial\Phi^l_{i,j,k}}{\partial z} + \frac{\partial P_y}{\partial z} \\
a^l_{z;i,j,k}\frac{\partial\Phi^l_{i,j,k}}{\partial x} + \frac{\partial P_z}{\partial x} & a^l_{z;i,j,k}\frac{\partial\Phi^l_{i,j,k}}{\partial y} + \frac{\partial P_z}{\partial y} & 1 + a^l_{z;i,j,k}\frac{\partial\Phi^l_{i,j,k}}{\partial z} + \frac{\partial P_z}{\partial z}
\end{bmatrix}.
$$

Let $Q \in \Omega^l_{i,j,k}$ and $\Delta_Q(\delta)$ be the Jacobian at Q as an affine function of δ. It should be noticed that Δ_Q may not be uniquely defined if Q lies at the border between two (or more) different $S^l_{p,q,r}$ boxes.

It is straightforward that $\Delta_Q(0) \in [J_m, J_M]$ since the vector a^l to be updated is the output of a previous updating scheme fulfilling the bounding condition on the Jacobian. Moreover, we have

$$\forall \delta \in \mathbb{R}^+ \quad J_M(\delta) = \sup_{[x,y,z]^t \in S^l_{p,q,r}} J(x,y,z,\delta) \geq \Delta_Q(\delta)$$
$$\Rightarrow \delta^+ \leq \arg_{\delta \geq 0} (\Delta_Q(\delta) = J_M).$$

Relation $\delta^+ \leq \arg_{\delta \geq 0} (\Delta_Q(\delta) = J_m)$ holds as well. It should be noticed that both arguments may simultaneously not exist. This is for example the case if the slope of Δ_Q is positive and J_M infinite.

Particular points of $\Omega^l_{i,j,k}$ have to be considered. We chose the eight vertices of each of the eight $S^l_{p,q,r}$ boxes.

C. Refinement Step

The current guess $[0, \delta_s^+]$ for the bracketing of δ^+ is refined by scanning $J_m(\delta)$ and $J_M(\delta)$ on each of the eight $S^l_{p,q,r}$ boxes according to the following algorithm.

Refinement step for the computation of δ^+
Purpose: tight bracketing $[\delta_i^+, \delta_s^+]$ of δ^+.
Initialization: $\delta_i^+ = 0$, δ_s^+ from the initialization step.
Method:
```
 loop on p,q,r          // see remark 1 below
  if (acknowledge (J_m) == false)
   make proposal (δ_i^+, δ_s^+) starting with
(0,δ_s^+)
    update δ_s^+
  end if
  if (acknowledge (J_M) == false)
   make proposal (δ_i^+, δ_s^+) starting with
(0,δ_s^+)
    update δ_s^+
  end if
 end loop on p,q,r.
```
Output:
δ_s^+ as its current value;
δ_i^+ as the infimum of all intermediate proposals on δ_i^+.

Remark 1: Particular attention is paid to the box which determines the initial guess: This box will be processed first and not considered for acknowledgment (*i.e.,* proposals will systematically be made). The goal is to make sure that δ_i^+ will not eventually be given a vanishing value and to reduce the computational burden: The odds are good that processing the other boxes will merely amount to going through the acknowledgment phase, hence avoiding the global optimization process which is time consuming.

Subprocedures: The algorithm is based on the following procedures. 1) *Acknowledgment:* Acknowledging J_m for a current value δ_s^+ must guarantee that $\forall \delta \in [0, \delta_s^+] \quad J_m \leq J_m(\delta)$. This condition is fulfilled if we have $J_m \leq J_m^-(\delta_s^+)$, which is the condition that will be checked. The condition has only to be checked for $\delta = \delta_s^+$ since it is necessarily true for $\delta = 0$ and since $J_m(\delta)$ is concave. 2) *Proposal:* δ_m^+ is bracketed, with an initial guess $[0, \delta_s^+]$ according to the iterative algorithm depicted in Fig. 12. 3) *Updating δ_s^+:* This means taking the infimum value between the current value and the proposal.

Output: The output of the algorithm is an interval bracketing δ^+. The lower bound δ_i^+ will be considered for the minimization of energy E.

Remark 2: The convergence of the procedure bracketing δ_m^+ toward its solution is guaranteed by the concavity of $J_m(\delta)$ (see Fig. 12). Convergence of the interval analysis algorithm (*i.e.,* bracketing $J_m(\delta)$ for a given δ) is guaranteed since each $S^l_{p,q,r}$ box is split into a finite number of subboxes ($S^l_{p,q,r}$ is of finite size and is split into subboxes which have a size larger than a user-defined limit).

APPENDIX III
OVERVIEW OF INTERVAL ANALYSIS

The goal of interval analysis techniques is to devise algorithms addressing for example global optimization problems, the resolution of systems of equations, or the characterization of sets defined by inequalities.

The main tools are basic operations based on intervals (possibly intervals in $\mathbb{R}^n$, which are called boxes) such as union, intersection, addition, product, inverse, inclusion functions and contractors. These techniques are convenient for problems of small dimensionality only (typically, up to 10) because of a rapidly growing computational burden.

In this section, we shortly describe some of the basic tools and the global optimization algorithm we used. We focus on polynomial cost functions which are the functions at hand. The reader is referred to [20], [23] for additional details.

A. Inclusion Functions

Let $\boldsymbol{x} \in [\boldsymbol{x}] \subset \mathbb{R}^n$, $[\boldsymbol{x}]$ being a box of the type $[\boldsymbol{x}] = [x_1^-; x_1^+] \times [x_2^-; x_2^+] \times \cdots$, and $f : [\boldsymbol{x}] \mapsto \mathbb{R}$ (notations are taken from [23]). An inclusion function $[f]$ on $[\boldsymbol{x}]$ is such that

$$\forall [\boldsymbol{x}] \subset \mathbb{R}^n f([\boldsymbol{x}]) \subset [f]([\boldsymbol{x}]).$$

In other words, an inclusion function $[f]$ on $[\boldsymbol{x}]$ is a function yielding an interval containing the image of $[\boldsymbol{x}]$ by f. We require the inclusion functions to be convergent: When $[\boldsymbol{x}]$ shrinks to a point, $[f]([\boldsymbol{x}])$ must shrink to a point as well.

Let us consider the example of a polynomial on $\mathbb{R}^n$

$$f : \mathbb{R}^n \longmapsto \mathbb{R}$$
$$\boldsymbol{x} \longmapsto f(\boldsymbol{x}) = a_0 + \sum_i a_i \left(\prod_j x_j^{n_{ij}} \right).$$
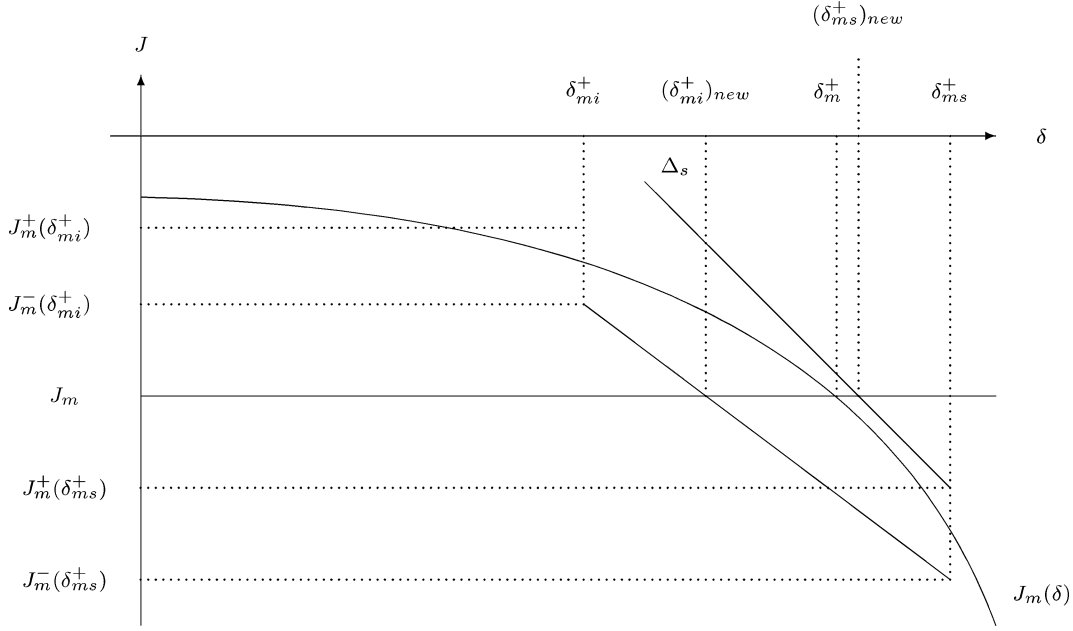
Fig. 12. Bracketing of δ_m^+. The affine function Δ_s is the Jacobian at the point $P(\delta_{ms}^+)$ as a function of δ. The lower bound δ_{mi}^+ is updated (*i.e.*, let $\delta_{mi}^+ \longleftarrow (\delta_{mi}^+)_{\text{new}})$ if $J_m^-((\delta_{mi}^+)_{\text{new}}) > J_m$; the upper bound δ_{ms}^+ is updated if $J_m^+((\delta_{ms}^+)_{\text{new}}) < J_m$. Iterations proceed until convergence (see Appendix III-C).

For the case at hand, *i.e.*, a polynomial defined on a box $[\boldsymbol{x}]$, we make a change of variable of the type $\tilde{\boldsymbol{x}} \triangleq \boldsymbol{x} - \boldsymbol{x}^-$, which yields a polynomial $\tilde{f}$. A possible choice for an inclusion function is

$$[f]([\boldsymbol{x}]) = \left[\tilde{f}\right]([\tilde{\boldsymbol{x}}]) = \left[\tilde{a}_0 + \sum_i \mathbb{1}_{(\tilde{a}_i < 0)} \tilde{a}_i \prod_j \left(\tilde{x}_j^+\right)^{n_{ij}} \right.$$

$$\left. \tilde{a}_0 + \sum_i \mathbb{1}_{(\tilde{a}_i > 0)} \tilde{a}_i \prod_j \left(\tilde{x}_j^+\right)^{n_{ij}} \right]$$

where $\mathbb{1}_{(.)}$ is the indicator function with values in $\{0, 1\}$. This is the inclusion function we used. There are many other possible choices for inclusion functions [23].

B. Contractors

A contractor is an algorithm replacing a box $[\boldsymbol{x}']$ by a smaller box $[\boldsymbol{x}'']$ still containing the solution of the problem. We considered the following contractor, among other possible choices.

Let us consider the variable x_1. The gradient component $\partial f/\partial x_1$ is an affine function (in the particular case of first-degree splines used here) of x_1 whose coefficients are polynomials in $x_2, x_3, \ldots$ that may be bracketed using inclusion functions. This yields $\partial f/\partial x_1 = a\, x_1 + b$, where $a \in [a_m, a_M]$ and $b \in [b_m, b_M]$ (see Fig. 13). For $x_1 \in \left[x_1^-, (x_1^-)_{\text{new}}\right[$, $\partial f/\partial x_1 < 0$. Hence, no minimum can be attained in the box $\left[x_1^-, (x_1^-)_{\text{new}}\right[\times [x_2^-, x_2^+] \times \cdots$ and x_1^- may be updated with $(x_1^-)_{\text{new}}$. Likewise, x_1^+ can be updated with $(x_1^+)_{\text{new}}$. The same scheme applies to $x_2, x_3, \ldots$ The procedure is repeated about ten times in a row.

C. Global Optimization

The branching algorithm achieving global optimization handles two lists of boxes [23, "OPTIMIZE" algorithm, p. 119]. $\mathcal{Q}$
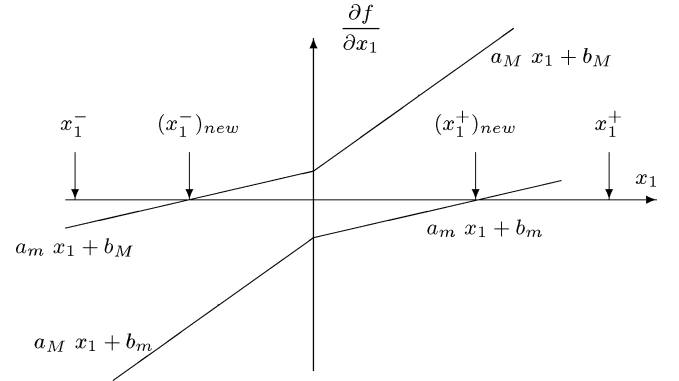

Fig. 13. Bracketing the gradient of f.

is a working list of boxes to be processed, in turn, $\mathcal{L}$ is a list of small size boxes, each of them possibly enclosing the global minimum of the cost function, $\overline{c}$ is an upper bound of the global minimum $\widehat{c}$ ($\overline{c}$ is updated as the algorithm proceeds). As an initialization, $\mathcal{Q}$ contains the initial box to be scanned, $\mathcal{L}$ is empty and $\overline{c} = +\infty$.

To process the list $\mathcal{Q}$ (iterate while $\mathcal{Q}$ is not empty).

- Pop a box $[\boldsymbol{x}]$ from $\mathcal{Q}$.
- Run a local optimization algorithm on $[\boldsymbol{x}]$ yielding $\check{\boldsymbol{x}}$ and $f(\check{\boldsymbol{x}})$.
- Let $\overline{c} = \inf \{\overline{c}, f(\check{\boldsymbol{x}})\}$.
- Split the box into subboxes (see **Appendix III-D**) and with each of those subboxes:
  - contract the box;
  - compute the inclusion function on the box;
  - throw the box away if the lower bound is larger than $\overline{c}$;

```
 – push the subbox in ℒ if the box is
smaller than a user-defined size;
 – if the subbox is still there, push it
in 𝒬.
```

Processing the list $\mathcal{L}$ amounts to computing an inclusion function on each (small–sized) box and eventually deriving an interval bracketing $\widehat{c}$ and a point P such that $f(P) \geq \widehat{c}$, $f(P)$ being equal to the upper bound on $\widehat{c}$.

D. Miscellaneous

In this section, we detail some particular options we took with a view to reducing the computation time.

1) The local iterative optimization algorithm retained is of Gauss–Seidel type. Each variable x_i is updated in turn till convergence. This is easy and fast, since the polynomials defining the Jacobian are quadratic in each variable.

2) Each local minimum reached using this procedure is enclosed in a subbox of minimal (user-defined) size and the larger box containing it is splitted along the subbox's hyperplanes (the larger box may be split into up to 27 subboxes).

3) We used only one type of inclusion function. It is more efficient to compute the bounds on the Jacobian on a box roughly (and fast) and to bisect more often than to compute more precise bounds and deal with less subboxes (this is due to the reduced dimensionality of the problem).

4) Reducing the size of the boxes (contraction) is very important regarding computation time.

ACKNOWLEDGMENT

REFERENCES

[1] N. Andreasen, R. Rajarethinam, T. Cizaldo, S. Arndt, V. Swayze, L. Flashman, D. O'Leary, J. Ehrhardt, and W. Yuh, "Automatic atlas-based volume estimation of human brain regions from MR images," *J. Comput. Assisted Tomogr.*, vol. 20, no. 1, pp. 98–106, 1996.

[2] J. Ashburner, J. Andersson, and K. Friston, "High-dimensional image registration using symmetric priors," *Neuroimage*, vol. 9, no. 6, pp. 619–628, Jun. 1999.

[3] ——, "Image registration using a symmetric prior – In three dimensions," *Human Brain Mapping*, vol. 9, no. 4, pp. 212–225, Apr. 2000.

[4] J. Ashburner and K. Friston, "Spatial normalization," in *Brain Warping*, A. W. Toga, Ed. New York: Academic, 1999, ch. 2, pp. 27–44.

[5] C. Baillard, P. Hellier, and C. Barillot, "Segmentation of brain 3D MR images using level sets and dense registration," *Med. Image Anal.*, vol. 5, no. 3, pp. 185–194, Sep. 2001.

[6] M. Bosc, F. Heitz, J.-P. Armspach, I.-J. Namer, D. Gounot, and L. Rumbach, "Automatic change detection in multimodal serial MRI: Application to multiple sclerosis lesion evolution," *Neuroimage*, vol. 20, no. 2, pp. 643–656, Oct. 2003.

[7] P. Cachier and D. Rey, "Symmetrization of the nonrigid registration problem using inversion-invariant energies: Application to multiple sclerosis," in *Proc. Medical Image Computing and Computer-Assisted Intervention, Lecture Notes in Computer Science*, vol. 1935, Pittsburgh, PA, Oct. 2000, pp. 472–481.

[8] M. Chen, T. Kanade, D. Pomerleau, and H. Rowley, "Anomaly detection through registration," *Pattern Recognit.*, vol. 32, no. 1, pp. 113–128, Jan. 1999.

[9] G. Christensen and H. Johnson, "Consistent image registration," *IEEE Trans. Med. Imag.*, vol. 20, no. 7, pp. 568–582, Jul. 2001.

[10] G. Christensen, S. Joshi, and M. Miller, "Volumetric transformation of brain anatomy," *IEEE Trans. Med. Imag.*, vol. 16, no. 12, pp. 864–877, Dec. 1997.

[11] G. Christensen, M. Miller, M. Vannier, and U. Grenander, "Individualizing neuro-anatomical atlases using a massively parallel computer," *IEEE Computer*, vol. 29, no. 1, pp. 32–38, Jan. 1996.

[12] G. Christensen, R. Rabbit, M. Miller, S. Joshi, U. Grenander, T. Coogan, and D. Van Essen, "Topological properties of smooth anatomic maps," presented at the 16th Int. Conf. Information Processing in Medical Imaging, Ile de Berder, France, Jun. 1995.

[13] G. Christensen, R. Rabbitt, and I. Miller, "Deformable templates using large deformation kinematics," *IEEE Trans. Image Process.*, vol. 5, no. 10, pp. 1435–1447, Oct. 1996.

[14] I. Dinov, M. Mega, P. Thompson, R. Woods, D. Sumners, E. Sowell, and A. Toga, "Quantitative comparison and analysis of brain image registration using frequency-adaptive wavelet shrinkage," *IEEE Trans. Inf. Technol. Biomed.*, vol. 6, no. 1, pp. 73–85, Mar. 2002.

[15] I. Dinov and D. Sumners, "Applications of frequency dependent wavelet shrinkage to analyzing quality of image registration," *SIAM J. Appl. Math.*, vol. 62, no. 2, pp. 367–384, Dec. 2001.

[16] J. Gee and D. Haynor, "Rapid coarse-to-fine matching using scale-specific priors," *Proc. SPIE Medical Imaging*, vol. 2710, pp. 416–427, 1996.

[17] J. Gee, M. Reivich, and R. Bajcsy, "Elastically deforming 3D atlas to match anatomical brain images," *J. Comput. Assisted Tomogr.*, vol. 17, no. 2, pp. 225–236, 1993.

[18] U. Grenander, *General Pattern Theory*. New York: Oxford Univ. Press, 1993.

[19] U. Grenander and M. Miller, "Computational anatomy: An emerging discipline," *Quart. Appl. Math.*, vol. 56, no. 4, pp. 617–694, Dec. 1998.

[20] E. Hansen, *Global Optimization using Interval Analysis*. New York: Marcel-Dekker, 1992.

[21] P. Hellier, C. Barillot, I. Corouge, B. Gibaud, G. Le Goualher, D. Collins, A. Evans, G. Malandain, N. Ayache, G. Christensen, and J. Johnson, "Retrospective evaluation of intersubject brain registration," *IEEE Trans. Med. Imag.*, vol. 22, no. 9, pp. 1120–1130, Sep. 2003.

[22] P. Hellier, C. Barillot, E. Memin, and P. Perez, "Hierarchical estimation of a dense deformation field for 3D-robust registration," *IEEE Trans. Med. Imag.*, vol. 20, no. 5, pp. 388–402, May 2001.

[23] L. Jaulin, M. Kieffer, O. Didrit, and E. Walter, *Applied Interval Analysis*. New York: Springer, 2001.

[24] S. Joshi and M. Miller, "Landmark matching via large deformation diffeomorphisms," *IEEE Trans. Image Process.*, vol. 9, no. 8, pp. 1357–1370, Aug. 2000.

[25] U. Kjems, S. Strother, J. Anderson, I. Law, and L. Hansen, "Enhancing the multivariate signal of [O-15] water PET studies with a new nonlinear neuroanatomical registration algorithm," *IEEE Trans. Med. Imag.*, vol. 18, no. 4, pp. 306–319, Apr. 1999.

[26] J. Kybic and M. Unser, "Multidimensional elastic registration of images using splines," in *Proc. IEEE Int. Conf. Image Processing*, vol. II, Vancouver, BC, Canada, Sep. 2000, pp. 455–458.

[27] ——, "Fast parametric elastic image registration," *IEEE Trans. Image Process.*, vol. 12, no. 11, pp. 1427–1442, Nov. 2003.

[28] L. Lemieux, U. Wieshmann, N. Moran, D. Fish, and S. Shorvon, "The detection and significance of subtle changes in mixed-signal brain lesions by serial MRI scan matching and spatial normalization," *Med. Image Anal.*, vol. 2, no. 3, pp. 227–242, 1998.

[29] S. Mallat, *A Wavelet Tour of Signal Processing*. New York: Academic, 1998.

[30] J. Martin, A. Pentland, S. Sclaroff, and R. Kikinis, "Characterization of neuropathological shape deformations," *IEEE Trans. Pattern Anal. Mach. Intell.*, vol. 20, no. 2, pp. 97–112, Feb. 1998.

[31] M. Miller, S. Joshi, and G. Christensen, "Large deformation fluid diffeomorphisms for landmark and image matching," in *Brain Warping*, A. W. Toga, Ed. New York: Academic, 1999, ch. 7, pp. 115–131.

[32] M. Miller and L. Younes, "Group actions, homeomorphisms, and matching: A general framework," *Int. J. Comput. Vis.*, vol. 41, no. 1/2, pp. 61–84, 2001.

[33] O. Musse, F. Heitz, and J.-P. Armspach, "3D deformable image matching using multiscale minimization of global energy functions," in *Proc. IEEE Conf. Computer Vision and Pattern Recognition*, vol. 2, Fort Collins, CO, 1999, pp. 478–484.

[34] ——, "Topology preserving deformable image matching using constrained hierarchical parametric models," *IEEE Trans. Image Process.*, vol. 10, no. 7, pp. 1081–1093, Jul. 2001.

[35] ——, "Fast deformable matching of 3D images over multiscale nested subspaces. Application to atlas-based MRI segmentation," *Pattern Recognit.*, vol. 36, no. 8, pp. 1881–1899, 2003.

[36] C. Nikou, G. Bueno, F. Heitz, and J.-P. Armspach, "A joint physics-based statistical deformable model for multimodal brain image analysis," *IEEE Trans. Med. Imag.*, vol. 20, no. 10, pp. 1026–1037, Oct. 2001.

[37] G. Subsol, N. Roberts, M. Doran, J.-P. Thirion, and G. Whitehouse, "Automatic analysis of cerebral atrophy," *Magn. Res. Imag.*, vol. 15, no. 8, pp. 917–927, 1997.

[38] R. Szeliski and J. Coughlan, "Spline-based image registration," *Int. J. Comput. Vis.*, vol. 22, no. 3, pp. 199–218, Mar.-Apr. 1997.

[39] J.-P. Thirion, "Image matching as a diffusion process: An analogy with Maxwell's demons," *Med. Image Anal.*, vol. 2, no. 3, pp. 243–260, 1998.

[40] ——, "Diffusing models and applications," in *Brain Warping*, A. W. Toga, Ed. New York: Academic, 1999, ch. 9, pp. 143–155.

[41] P. Thompson, J. Giedd, R. Woods, D. MacDonald, A. Evans, and A. Toga, "Growth patterns in the developing brain detected by using continuum-mechanical tensor maps," *Nature*, vol. 404, no. 6774, pp. 190–193, Mar. 2000.

[42] P. Thompson, D. MacDonald, M. Mega, C. Holmes, A. Evans, and A. Toga, "Detection and mapping of abnormal brain structure with a probabilistic atlas of cortical surfaces," *J. Comput. Assisted Tomogr.*, vol. 21, no. 4, pp. 567–581, 1997.

[43] P. Thompson and A. Toga, "Anatomically driven strategies for high-dimensional brain image warping and pathology detection," in *Brain Warping*, A. W. Toga, Ed. New York: Academic, 1999, ch. 18, pp. 311–336.

[44] ——, "Warping strategies for intersubject registration," in *Handbook of Medical Imaging. Processing and Analysis*, I. N. Bankman, Ed. New York: Academic, 2000, ch. 36, pp. 569–601.

[45] P. Thompson, R. Woods, M. Mega, and A. Toga, "Mathematical/computational challenges in creating deformable and probabilistic atlases of the human brain," *Human Brain Mapping*, vol. 9, no. 2, pp. 81–92, Feb. 2000.

[46] A. Toga and P. Thompson, "An introduction to brain warping," in *Brain Warping*, A. W. Toga, Ed. New York: Academic, 1999, ch. 1, pp. 1–26.

[47] A. Trouvé, "Diffeomorphisms groups and pattern matching in image analysis," *Int. J. Comput. Vis.*, vol. 28, no. 3, pp. 213–221, Jul.-Aug. 1998.

[48] Y. Wu, T. Kanade, C. Li, and J. Cohn, "Image registration using wavelet-based motion model," *Int. J. Comput. Vis.*, vol. 38, no. 2, pp. 129–152, Jul. 2000.

Vincent Noblet received the Engineer degree in physics from the Ecole Nationale Superieure de Physique de Strasbourg, Strasbourg, France, in 2002. He is currently pursuing the Ph.D. degree at the Université Louis Pasteur (Laboratoire des Sciences de l'Image, de l'Informatique et de la Teledetection, UMR CNRS-ULP 7005), Strasbourg, France.

His research interests include medical image analysis and deformable models.

Christian Heinrich received the Engineer degree in electrical engineering from Supelec, Paris, France, in 1990 and the Ph.D. degree from the University of Paris-Sud, Orsay, France, in 1997.

He is now an Assistant Professor at the Ecole Nationale Superieure de Physique de Strasbourg, Strasbourg, France. He is also with the Laboratoire des Sciences de l'Image, de l'Informatique et de la Teledetection, UMR CNRS-ULP 7005, Strasbourg.

His research interests include image registration, inverse problems, and statistical image modeling.

Fabrice Heitz received the Engineer degree in electrical engineering and telecommunications from Telecom Bretagne, Bretagne, France, in 1984 and the Ph.D. degree from Telecom Paris, Paris, France, in 1988.

From 1988 until 1994, he was with INRIA, Rennes, France, as a Senior Researcher in image processing and computer vision. He is now a Professor at Ecole Nationale Superieure de Physique, Strasbourg, France (Image Science, Computer Science and Remote Sensing Laboratory LSIIT UMR CNRS 7005). His research interests include statistical image modeling, image sequence analysis, and medical image analysis.

Prof. Heitz was an Associate Editor for the IEEE TRANSACTIONS ON IMAGE PROCESSING from 1996 to 1999. He is currently Assistant Director of LSIIT.

Jean-Paul Armspach received the Engineer degree from INSA Lyon, Lyon, France, in 1978 and the Ph.D. degree from Louis Pasteur University, Strasbourg, France in 1992.

He is currently a Research Engineer at the Université Louis Pasteur (IPB, UMR-7004 CNRS-ULP), Strasbourg. His research interest are image sequence analysis and biomedical image processing.